Journal of the Optical Society of America B
OPTICAL PHYSICS

Three-dimensional photonic crystal short-pillar architecture for high-performance optical biosensing

DRAGAN VUJIC[1,2,3] AND SAJEEV JOHN[2,4]

[1]Faculty of Agronomy, University of Kragujevac, Cara Dusana 34, 32000 Cacak, Serbia
[2]Department of Physics, University of Toronto, 60 St. George St., Toronto, Ontario M5S 1A7, Canada
[3]e-mail: dvujic13@gmail.com
[4]e-mail: john@physics.utoronto.ca

Received 16 November 2020; accepted 16 January 2021; posted 25 January 2021 (Doc. ID 415100); published 25 February 2021

Numerical analysis of optical biosensors made of very short-pillar (only one or two lattice constants high) liquid-infiltrated photonic crystals is presented. The small pillar height makes these photonic crystals amenable to fabrication by techniques such as nanoimprinting. Our biosensors can detect at least three different analytes (disease markers), individually or combinatorially in a single spectroscopic measurement. The resonance linewidths of our proposed device are narrow enough to accurately identify the relative concentrations of analytes within the biofluid, enabling our device to provide both qualitative and quantitative disease diagnoses. The minimal volume of fluid sample required for diagnosis is set by the micrometer-scale lattice constant of the photonic crystal. Using finite-difference time-domain simulations, we present detailed spectral characteristics for all possible combinations of analyte attachment to the photonic crystal nanopillars.

https://doi.org/10.1364/JOSAB.415100

1. INTRODUCTION

Optical biosensors based on high-quality-factor localized modes offer an accurate, rapid, and simple method for medical diagnostics without time-consuming external laboratory testing. The functional principle of our optical biosensor is to detect the quantities of biomaterials accumulated along lines of nanopillars by resonant frequency shifts detected by light transmission measurements through a photonic crystal. To this end, certain internal surfaces of the device are coated with antibodies or DNA aptamers [1,2], leading to the binding of specific proteins from a sample of biological fluid. This selectively shifts resonances that are spatially localized within the region of the accumulated analytes, leading to reliable detection and discrimination of various diseases.

Photonic crystals [3,4] can completely prohibit light propagation over a range of frequencies known as the photonic band gap (PBG). As such they are ideal materials for creating subwavelength scale regions with strongly localized internal illumination. Strongly localized light regions are achieved by engineering defects inside the otherwise periodic structure of the photonic crystal. These defects allow light of certain frequencies (that we call resonant frequencies) to exist in certain hot spots within the photonic crystal. Since the resonant frequency depends on the geometric and dielectric structure of the defect, any change in the resonant frequency (due to flow of biofluid through photonic crystal) indicates deposits of analyte in the hot spot where light is localized. Numerous approaches based on photonic crystals can be found in the literature [5–8]. Other approaches to optical biosensing include surface plasmon resonances (SPR) [9], optical gratings [10], and waveguides [7,11]. The conceptual paradigm for biosensing using the PBG was described earlier [12,13]. This was followed by a full three-dimensional design using silicon nanopillars and interacting (hybridized) optical resonances [14].

Here we present a new three-dimensional PBG architecture suitable for multiparametric biosensing. Our architecture involves very high-quality-factor optical resonances within the PBG, well separated in frequency and realized by short nanopillars. Our proposed devices are well suited to modern manufacturing methods. Our first biosensor design consists of a photonic crystal with silicon nanopillars only two lattice constants high, making it amenable to mass production using techniques such as nanoimprinting. Furthermore, our device architecture facilitates very strongly localized optical modes within selected regions where analytes bind, resulting in high sensitivity. Finally, with remarkably small pillar heights, we demonstrate optical modes with very high Q factors. Consequently, very small changes in the resonance positions caused by very small amounts of bound analyte are clearly noticeable, so detection of disease markers is reliable and accurate. In other words, our devices have low limit of detection.

Our present design differs from previous PBG-based biosensors [12–14] that involve more complex, analyte-induced hybridization of resonant modes and surface modes, leading to complex spectral fingerprints. In these previous designs, all detection modes fall within a frequency band $\Delta\omega$ such that $\Delta\omega/\omega_0 \approx 3\%-4\%$, where ω_0 is the band center frequency. While this enables the use of relatively small-bandwidth light sources and detectors, it also leads to strong interaction between optical resonances and requires the use of longer nanopillars. Our present design utilizes a broader bandwidth $\Delta\omega/\omega_0 \approx 10\%$. This avoids mode hybridization and enables higher optical Q factors with shorter nanopillars. The trade-off is the requirement for a broader-band light source and detector.

This paper is organized as follows. In Section 2, we present a three-dimensional photonic crystal architecture with nanopillar height equal to twice the lattice constant. This exhibits three well-separated optical resonances acting independently of one another in the presence of analytes. Here we also explain the numerical simulation method used in this study. In Section 3, we present numerical results for various biomarker detections. We also discuss the sensitivity and the limit of detection of our device. In Section 4, we present a photonic crystal biosensor with reduced nanopillar height equal to just one single lattice constant and demonstrate its efficacy. In Section 5 we provide discussion and conclusions.

2. DESIGN OF A PBG-BASED MULTIPARAMETRIC BIOSENSOR

We consider a realistic three-dimensional photonic crystal consisting of short nanopillars as a potential multiparametric biosensor. Our three-dimensional biosensor actually consists of a two-dimensional photonic crystal made of high-dielectric rods, arranged in a square lattice, immersed in liquid. The vertical dimension of the photonic crystal and appropriate defects (deviations from perfect periodicity) on the dielectric rods are chosen to induce well-localized optical resonances, with high quality factors, within the PBG of the biosensor. Several spatially separated and noninteracting resonances allow detection of different concentrations of multiple disease markers in a single measurement. High sensitivity and low detection limits are ensured with strongly localized optical resonances that overlap the regions of analyte binding with high quality factors. An important feature of our biosensor is that while modes are strongly localized in the direction of light transmission, they are extended along the direction of the biofluid flow [12–14]. In other words, our optical resonances are waveguide modes rather than point-localized modes within the PBG. This greatly enhances the speed of biomarker detection since binding sites are available all along the analyte flow path. In the mouse-trap analogy, this minimizes the time required for the mouse to find its trap.

Our structure consists of just seven unit cells of silicon photonic crystal along the direction of light propagation. Due to the PBG, light transmission occurs through a "tunneling" type process rather than standard propagation. The radius of the circular-cross-section, silicon rods (nanopillars) is chosen as $r = 0.25a$, where a is the photonic crystal lattice constant. For clarity, each line of dielectric rods in the direction of light propagation is called a row, while each line in the direction of the fluid flow is called a column. The height of nanopillars in the z direction, orthogonal to fluid flow (y direction) and light propagation (x direction), will also be referred to as the vertical dimension (or the height) of the photonic crystal. In the middle and last columns of the structure, instead of circular-cross-section dielectric rods, we introduce elliptical-cross-section rods, with semiminor axes of 0.15a, oriented in the direction of light propagation. In every second row of dielectric rods, we introduce elliptic dielectric rods with semimajor axes of 0.30a for the middle column and 0.35a for the rear column. In every alternate second row, the elliptic dielectric rods have semimajor axes of 0.25a for the middle column, while the rods have elliptic semimajor axes of 0.40a for the rear column. This is presented in detail in Fig. 1. In this way, the structure is "period doubled" along the fluid flow direction, enabling an incident plane wave (traveling in the x direction) to couple to the waveguide modes within the PBG. These cross-sectional shape changes constitute what we call "defects" to the otherwise pristine photonic crystal in which all rods would have circular cross sections with $r/a = 0.25$. The defective middle and last columns, described above, are sufficient to engineer two separately localized and independent optical resonance modes. A third independent resonance mode is engineered by enlarging all silicon rods in the first column of the structure to the modified radius of $r = 0.35a$. This photonic crystal structure stands on a glass substrate. A fluid flow channel for biomarkers is created using tall vertical glass walls at a distance of 1.5a from the middle of the first and last dielectric columns. In the vertical direction, the system is unconstrained, which simplifies the flow of fluid within the periodic structure and reduces the possibility of clogging of large impurities in the fluid sample. This design with a large liquid region above the photonic crystal is called an open-top design [14]. At a suitable height, the flow channel may be covered with glass or other transparent solid material. Such a covering facilitates the movement of biomarkers by flow pressure in the fluid channel. The cover, made of a transparent low-index material, is chosen sufficiently high above the nanopillars to minimize the impact of light reflection from the cover itself. The direction of fluid flow, orthogonal to the light propagation, contains a very large number of photonic crystal unit cells to

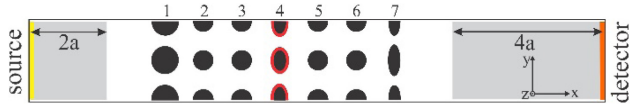

Fig. 1. Top view of biosensor. Standard photonic crystal structure, made of dielectric rods with radius $r = 0.25a$. Three defect columns are made according to following pattern: in the first column, all dielectric rods are enlarged and have radius of $r = 0.35a$. In the fourth and the last (seventh) column, dielectric rods have elliptic cross sections with semiminor axes of 0.15a oriented in the light propagation direction. In the fourth column, the outer elliptic dielectric rods have semimajor axes of 0.30a while the semimajor axis of the inner elliptic rod is 0.25a. In the seventh column, the outer elliptic dielectric rods have semimajor axes of 0.35a while the semimajor axis of the inner elliptic rod is 0.40a. The red coating on the central column depicts an absorbed layer of analyte that modifies the optical transmission spectrum and enables biomarker detection. More generally, different analytes may bind to three columns: on the surfaces of all dielectric rods in the second, fourth, or seventh columns of the photonic crystal.

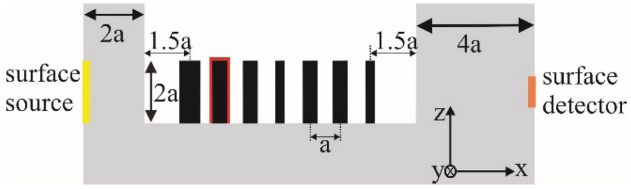

Fig. 2. Side view of biosensor: the analyte layer (depicted in red) is placed both around and above the defect rods. All nanopillars have height of 2a. A detector of vertical length 1a is aligned to the middle of the nanopillars. The height of the source is the same as the height of the nanopillars. The overall distance from source to detector is 15a.

minimize leakage of light into the vertical direction. We model this as an infinitely periodic system in the y direction, with a unit cell consisting of two rows of dielectric rods. We then apply periodic boundary conditions in the y direction. In all other directions we apply absorbing boundary conditions to prevent light reflection from the ends of the computational volume. For our computational purposes, we place our light source two unit cells into the glass wall. We assume that every mesh point, near the light source surface, up to the height of the nanopillars, injects light in every time step (see Fig. 2). The incident light has the form of a short Gaussian pulse at the beginning of the simulation. On the other (back) side, along the direction of light propagation, the spectrum is measured at a depth of 4a in the opposite glass wall. The extraction of a detected light spectrum requires Fourier transformation of the fields at every mesh point of the detector surface and requires considerable computational time. Our detector, located four unit cells deep within the rear glass wall, covers the $y-z$ area of 2a × a, and it is placed such that its midline coincides with mid-height of the nanopillars. In the y direction, our detector covers the whole computational area (see Figs. 1 and 2). According to a number of our trial simulations, this choice of detector provides an excellent rendition of transmitted light. The coordinate system is positioned so that the x axis indicates the direction of light propagation, the y axis coincides with the flow direction of biological fluid, and the z axis is directed vertically, orthogonal to the glass substrate.

The height of our structure is 2a, but the height of the surrounding glass is higher (see Fig. 2) in order to guide fluid flow. Computations are done with resolution of 12 × 12 × 12 pixels per unit cell. In order to increase the accuracy of our numerical simulations, we perform subpixel averaging of the dielectric constant inside the small volume associated with one mesh point. We compared the results obtained with this method to the results done with higher resolution to confirm the accuracy of our method. The simulation of the biosensor is done by solving Maxwell's curl equations in three dimensions using the Yee algorithm [15,16]. In order to detect the spectrum of light transmitted by the photonic crystal, we Fourier transform all the electric and magnetic fields oscillating orthogonally to the light propagation at every mesh point on the detector. We calculate the energy spectrum by integrating the real part of the x-component Poynting vector through the detector, and we calculate the transmission spectrum $T(\omega)$ as the ratio between the spectrum of the transmitted pulse and the spectrum of the incident pulse. The input pulse spectrum is defined and calculated by propagating the input pulse through the same computational volume filled with glass only. This pulse is initiated with the same source, and the pulse spectrum is measured with the same detector. In this definition of $T(\omega)$, it is possible for transmission peak values to exceed unity in cases where the photonic crystal guides more light into the detector than if the entire volume is filled with glass.

In our numerical simulation, we assume the silicon refractive index to be $n_{silicon} = 3.4$. The silicon nanopillars are immersed in a fluid containing biomarkers with refractive index assumed to be $n_{fluid} = 1.35$. The refractive index of the glass is taken as $n_{glass} = 1.5$. When the biomarkers bind to the silicon pillars to form a solid analyte, the coating layer is assumed to have refractive index $n_{analyte} = 1.45$. These values have been used previously [12,13] and are considered realistic [17]. Our simulations reveal narrow resonance line shapes with full width at half-maximum (FWHM) below 0.00005 ($2\pi c/a$). The majority of our simulations are performed with 1,500,000 finite-difference time-domain (FDTD) time steps. The transmission spectrum corresponding to Figs. 1 and 2, in the absence of analyte binding, is given in Fig. 3. This structure allows light to propagate through the PBG at three different and well-separated resonance frequencies. Consequently, this biosensor is able to detect three different biomarkers in a very simple and reliable way, without mode interaction and hybridization [12–14]. These three resonances are positioned at (i) $0.2930523(2\pi c/a)$ with FWHM of $0.000029(2\pi c/a)$ and Q factor of 10500, (ii) $0.278481(2\pi c/a)$ with FWHM of $0.000044(2\pi c/a)$ and Q factor of 6300, and (iii) $0.2687003(2\pi c/a)$ with FWHM of $0.000014(2\pi c/a)$ and Q factor of 19000 (see Fig. 3). These high quality factors provide a low limit of detection for the device. The corresponding two-dimensional photonic crystal, made of high dielectric material with a refractive index of $n_{silicon} = 3.4$, embedded in a fluid with $n_{fluid} = 1.35$, has a PBG in the frequency interval $0.25 < 2\pi c/a < 0.31$. It follows that the observed 3D resonances are located deep inside the PBG of the underlying 2D photonic crystal.

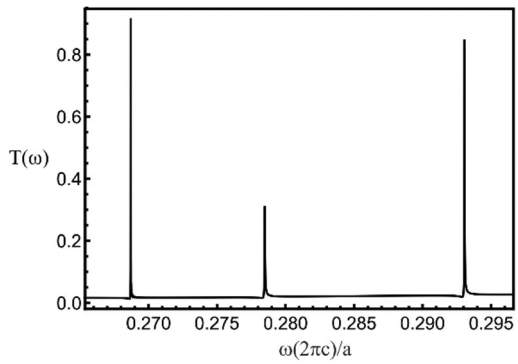

Fig. 3. Transmission spectrum of the biosensor depicted in Figs. 1 and 2, in the absence of analyte binding. The transmitted spectrum $T(\omega)$ is calculated as the ratio of the spectrum detected with photonic crystal (shown in Figs. 1 and 2) and the spectrum detected in a control system with all silicon pillars and biofluid replaced with glass everywhere. The photonic crystal architecture reveals a spectral fingerprint containing three well-separated resonances at 0.2930523, 0.278481, and 0.2687003 ($2\pi c/a$) with mutually independent responses to analyte adsorption.

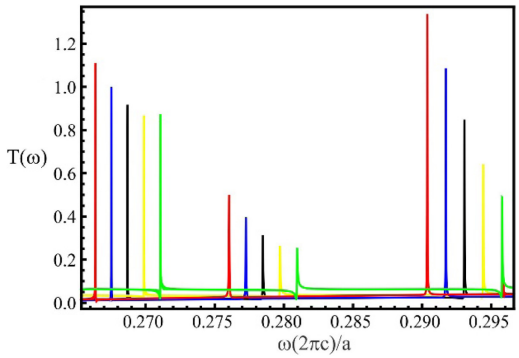

Fig. 4. Transmission spectra of the biosensor, without surface functionalization by antibodies or DNA aptamers, for different values of the background fluid refractive index n_{fluid}. The green line corresponds to $n_{fluid} = 1.300$, the yellow line to $n_{fluid} = 1.325$, the black line to the assumed value of $n_{fluid} = 1.350$ (as in Fig. 3), the blue line to $n_{fluid} = 1.375$, and the red line to $n_{fluid} = 1.400$. Higher background fluid index leads to a downshift of all resonance frequencies accompanied by an increase in peak intensity. Lower background fluid index leads to an increase of all resonance frequencies but a decrease of peak intensities.

It is possible that the average fluid refractive index, $n_{fluid} = 1.35$, may fluctuate due to undesirable impurities, so it is important to know the behavior of the resonance modes due to the slight change of fluid refractive index. In Fig. 4 we present the transmission spectra of our biosensor for five separate values of the background fluid refractive index $\{n_{fluid} \in 1.300, 1.325, 1.350, 1.375, 1.400\}$. Figure 4 reveals that all resonances have very similar frequency displacements due to the change in the refractive index of the fluid. In order to eliminate possible misinterpretation of results due to the possible fluctuation of the overall fluid refractive index, it is important to measure the spectral fingerprint of the structure in the absence of antibodies or DNA aptamers that functionalize the silicon nanopillars to bind analyte molecules. This is important to distinguish the outcome in which three analytes bind to each of their binding sites from the false positive caused by an overall change in background fluid index. In the case of the long-pillar biosensor described previously [14], the elimination of this false positive was through the use of "index-guided bulk modes" (IGBMs) that respond directly to fluid background fluctuations independent of strongly localized optical resonances. In the present short-pillar biosensor, the change in transmission peak height provides the required distinction. In the case of background fluid index increase, all transmission peak heights likewise increase. This is distinguishable from analyte binding [see Fig. 10(d)].

3. SPECTRAL FINGERPRINTS FOR BIOMARKER IDENTIFICATION

The amount of analyte adsorbed on selected nanopillars determines the shift of resonant frequency from the baseline frequencies shown in Fig. 3. This enables detection of both the type and amount of analyte adsorbed in different nanopillar columns of the photonic crystal. We first perform a numerical simulation to determine the spatial distribution of light at each of the resonant frequencies shown in Fig. 3. Based on the local

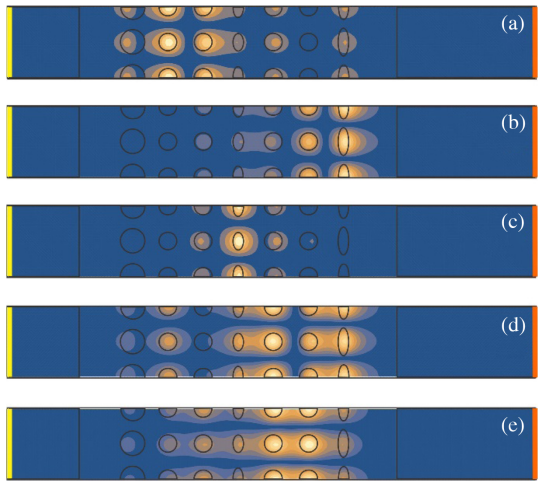

Fig. 5. Resonant illumination intensity patterns at the nanopillar mid-height of the photonic crystal structure. (a) Square of electric field amplitude (time averaged over one optical cycle) of light oscillating at frequency 0.2687003 ($2\pi c/a$) inside the structure. Since the most illuminated are rods in column 2, we functionalize this column to bind the first analyte. (b) Intensity of light oscillating at frequency 0.278481 ($2\pi c/a$). For this frequency the elliptic rods in column 7 are functionalized to bind a second (distinct) analyte. (c) Intensity of light oscillating at frequency 0.2930523 ($2\pi c/a$). The most illuminated are elliptic rods in column 4 (center of photonic crystal). Nanopillars in column 4 are functionalized to bind the third analyte distinct from the previous two. The two resonant illuminations presented in parts (d) and (e) are not chosen to be operating modes. (d) Intensity of light oscillating at frequency 0.262151($2\pi c/a$). (e) Intensity of light oscillating at frequency 0.247326 ($2\pi c/a$).

distribution of resonant light near each dielectric rod, we select the most efficacious rods for functionalization and subsequent analyte binding. Each resonant frequency is sensitive only to analyte binding in regions illuminated by that resonant light. We then study the spectral fingerprints of the transmitted light with the analyte adsorbed to each of the functionalized rods separately and to all possible combinations of functionalized rods. For a more detailed picture we provide simulations, in each case, for three different coating thicknesses of the adsorbed analyte.

In Fig. 5, we present resonant field intensity patterns at mid-height on the nanopillars for three chosen resonances. In order to confirm that light is fully localized in all directions around the selected rods, we present a side-view slice of the resonant light illumination in Fig. 6, where the slice cuts through the middle of a nanopillar row. Figures 5 and 6 reveal that the spatial illumination overlap of these three separate resonant frequencies is marginal. Accordingly, we expect an independent response to each different analyte adsorption.

We functionalize our biosensor by attaching three different types of antibodies or DNA aptamers around all rods in the second, fourth, and seventh columns of the photonic crystal. The functionalization of analyte binding surfaces might be realized by high-resolution 3D inkjet printing [18,19]. The dielectric rods in the selected columns can then bind three different targeted proteins (markers) either separately or in all possible combinations, depending on the nature and extent

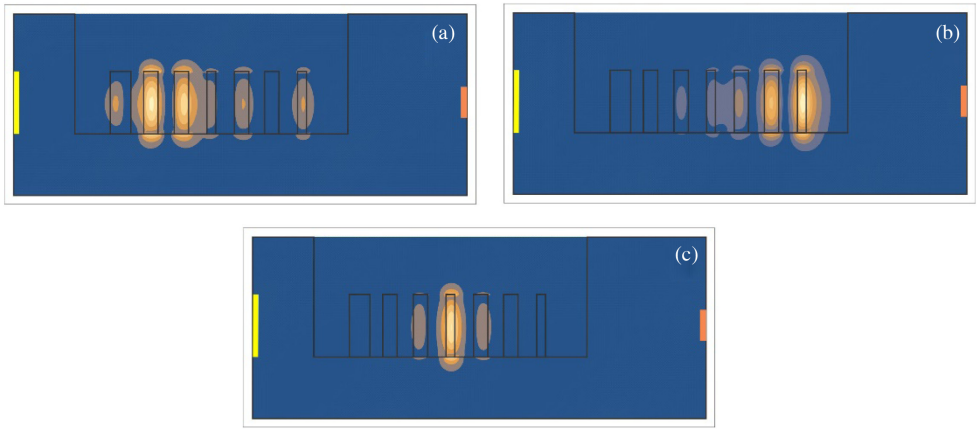

Fig. 6. Side view of resonant illumination of the device. Vertical slices of intensity pattern of light oscillating at frequencies (a) 0.2687003 ($2\pi c/a$), (b) 0.278481 ($2\pi c/a$), and (c) 0.2930523 ($2\pi c/a$) corresponding to the horizontal slices shown in Fig. 5. Each planar slice cuts the photonic crystal through the center of a row of nanopillars.

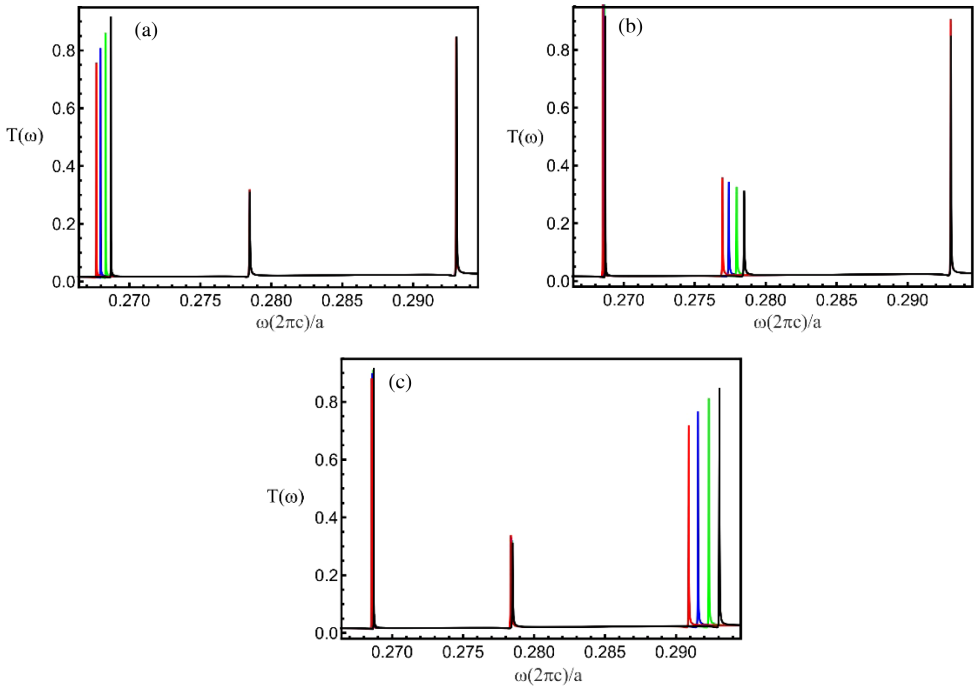

Fig. 7. Transmission resonance shifts for various analyte coating thicknesses: black line, without analyte; green line, 0.05a coating thickness of analyte; blue line, 0.1a layer of analyte; and red line, 0.15a layer of analyte. Various biomarker coating thicknesses are located around nanopillars in the (a) second, (b) seventh, and (c) fourth columns of the photonic crystal.

of a disease. This is then detected by the change in optical resonances. Figures 5 and 6 also reveal the strong optical overlap of the electromagnetic field with the region of analyte surface binding. This promises high sensitivity of the biosensor.

In Fig. 5(d) and 5(e), we present two other optical resonances at frequencies below the spectral range shown in Figs. 3 and 4. However, given the narrow linewidths of our resonances and the magnitude of analyte-induced shifts (see below), there is no likelihood of interaction (or hybridization) between the modes of Figs. 5(d) and 5(e) with the modes utilized for biosensing as illustrated in Figs. 5(a)–5(c). Consequently, the modes depicted in Figs. 5(d) and 5(e) will not be analyzed further in this paper.

In order to capture the contributions from the various resonances in Fig. 5, we study the transmission of broadband input pulses through the PBG and examine the resulting spectral fingerprints. This transmission is made possible through our carefully engineered defect architecture. The change in transmission with different layer thicknesses of bound analyte around the second column is presented in Fig. 7(a). Transmission without the analyte adsorbed is presented with black color. The green, blue, and red curves correspond to 0.5a, 0.1a, and 0.15a thick layers of analyte, respectively. Figure 7(a) also reveals that analyte binding to the second column leaves the transmission resonances at frequencies of 0.278481 ($2\pi c/a$) and 0.2930523 ($2\pi c/a$) unaffected. Only resonant transmission at 0.2687003

Table 1. Shifts of the Corresponding Resonances Measured in Units ($2\pi c/a$) and in Units of Resonant Bandwidth Indicated by $\Delta\omega_0$ in the Table[a]

Rods with Analyte in	Relevant ω_0	Relevant $\omega_{0.05}$	$\omega_0 - \omega_{0.05}$	Relevant $\omega_{0.15}$	$\omega_0 - \omega_{0.15}$	$\Delta\omega_0$ at Half Max. (FWHM)
Second column	0.2687003	0.2683305	0.0003698 25.7 $\Delta\omega_0$ (0.002a)	0.2676702	0.0010301 71.5 $\Delta\omega_0$ (0.0021a)	0.000014
Seventh column	0.278481	0.277953	0.000528 11.86 $\Delta\omega_0$ (0.0042a)	0.276952	0.001529 34.36 $\Delta\omega_0$ (0.00436a)	0.000044
Fourth column	0.2930523	0.292313	0.0007393 25.94 $\Delta\omega_0$ (0.002a)	0.290895	0.0021573 75.69 $\Delta\omega_0$ (0.002a)	0.000029

[a]We include (in brackets) the thickness of the analyte layer required to shift the resonant peak by one further FWHM from the presented shift in table columns 4 and 6.

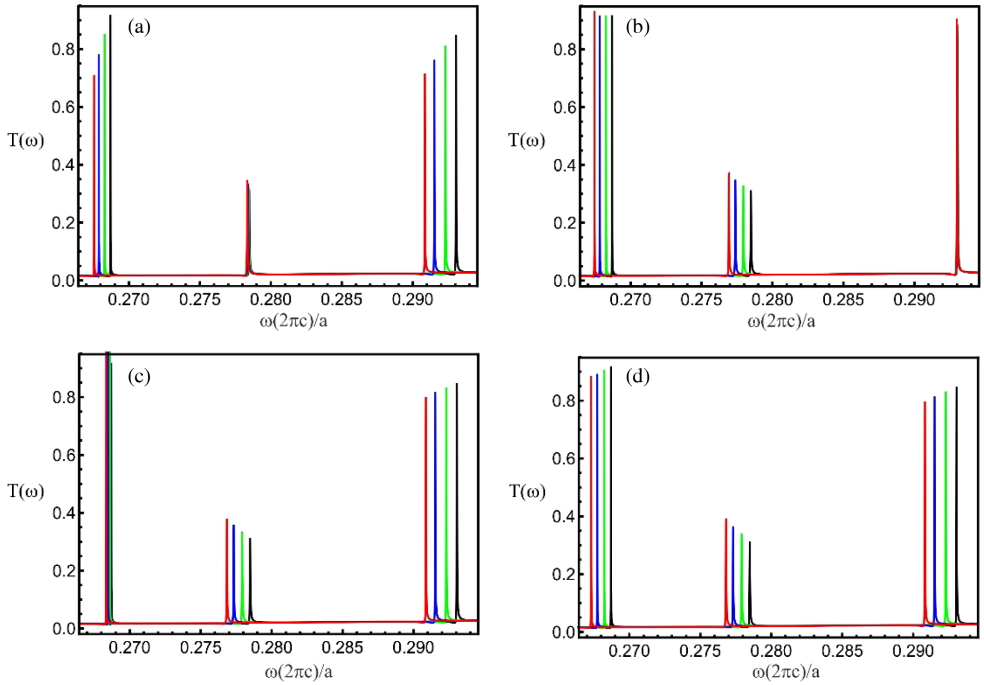

Fig. 8. Transmission resonance peaks of light localized within the PBG for various coating thicknesses of analyte around dielectric rods in (a) the second and fourth columns, (b) the second and seventh columns, (c) the fourth and seventh columns, and (d) the second, fourth, and seventh columns. Black line, without analyte; green line, rods with 0.05a layer thickness of analyte; blue line, rods with 0.1a coating thickness of analyte; and red line, rods with 0.15a layer thickness of analyte.

($2\pi c/a$) shifts, identifying both the position and amount of the analyte captured by the biosensor. The layer thickness provides an estimate of the marker concentration inside the solution. Similarly, for analyte binding to the seventh column, only the transmission resonance at frequency 0.278481 ($2\pi c/a$) is affected. The other two transmission peaks at 0.2687003 ($2\pi c/a$) and 0.2930523 ($2\pi c/a$) do not show perceptible interaction with analyte bound to the seventh column [see Fig. 7(b)]. Figure 7(c) depicts our numerical results for different levels of analyte bound to nanopillars in the fourth column. In this situation, only the transmission resonance at frequency 0.2930523 ($2\pi c/a$) has an observable shift due to binding of analyte to the fourth column of the photonic crystal.

We now examine the sensitivity and limit of detection of our biosensor. Table 1 lists resonant frequencies, linewidths, and lineshifts for a biosensor coated with 0.0a, 0.05a, and 0.15a thick layers of biomarkers. Resonant lineshifts are presented both in units of ($2\pi c/a$) and in units of the resonance bandwidths in order to estimate the amount of analyte needed to shift the resonance by one FWHM. This is an indicator of the limit of detection of our biosensor. From Table 1, it is apparent that the central resonance at $\omega_0 = 0.278481$ ($2\pi c/a$) has the largest linewidth and requires an analyte coating thickness of about 0.004a (to bind to the seventh column) to shift the resonance by one FWHM. The other two resonances require slightly thinner analyte layers in order to satisfy the detection criterion. Roughly speaking, an analyte thickness of 0.005a represents the limit of detection. If we restrict sensing to only dielectric rods in the second and fourth columns, the detection limit is slightly smaller.

In the case of two or three distinct biomarkers in the solution, we examine all their possible combinations with different coating layer thicknesses of analyte around selected dielectric rods. The optical transmission spectra in the case of two and three markers in the solution are given in Fig. 8. Here different colors represent different thicknesses of analyte coating around the selected rods. Green corresponds to 0.05a, blue corresponds to 0.1a, and red corresponds to 0.15a thick layers of the selected analyte. Black represents transmission in the absence of any analyte binding. In our numerical simulations presented in Fig. 8, we assume that the coating thicknesses of adsorbed biomarkers, when present, are the same for a given color. Since the shifts of different resonance peaks are largely independent, it is easy to infer the transmission spectra with different coating thicknesses in different columns.

Figure 8(a) presents analyte binding to the second and fourth columns of the photonic crystal. When the bound analyte layer thickness in the second column is 0.05a and the analyte thickness in the fourth column is 0.15a, the transmission resonance at 0.2687003 ($2\pi c/a$) shifts (green) to 0.26829 ($2\pi c/a$) while the resonance at 0.2930523 ($2\pi c/a$) shifts (red) to 0.2908546 ($2\pi c/a$). The transmission peak at 0.278481 ($2\pi c/a$) has no shift, confirming the absence of biomarker attachment in the seventh column of the structure. To test the independence of different biomarker attachments, we show in Fig. 9 (with blue), the peak shifts when one biomarker coating thickness in the second column is exactly 0.05a while a second biomarker layer thickness in the fourth column is exactly 0.15a. As expected, we obtain different peak shifts. However, the peak shifts are not identical to those depicted in Fig. 8(a) where each curve (of a given color) has the same analyte coating thickness in columns 2 and 4. This very small difference arises because the optical modes in Figs. 5(a) and 5(c) are not completely spatially separated. But the shifts are very similar. The resonance at 0.2687003 ($2\pi c/a$) shifts to 0.2681925 ($2\pi c/a$) instead of 0.2682905 ($2\pi c/a$), corresponding to the green curve in Fig. 8(a) or 0.2683305 ($2\pi c/a$) as suggested in Table 1 for only one column coated with biomarkers. Likewise, the resonance at 0.2930523 ($2\pi c/a$) shifts to 0.290882 ($2\pi c/a$) instead of 0.290895($2\pi c/a$) as suggested in Table 1. Similar considerations apply in the case of the oppositely chosen analyte thicknesses on the rods in columns two and four as represented by the green line in Fig. 9. This typifies the very small degree of interaction between analyte associated with one resonance mode and a different resonance mode. This is very different from the mode hybridization effect seen in previous designs [12–14].

The spectral fingerprints of analyte binding to the second and seventh columns are presented in Fig. 8(b). As expected, the resonant frequencies 0.2687003 ($2\pi c/a$) and 0.278481 ($2\pi c/a$) shift almost independently of each other. The spectra presented in Fig. 8(b) are very similar to what could be inferred from Figs. 7(a) and 7(b) for individual analytes. Light oscillating at 0.2930523 ($2\pi c/a$) is very tightly localized to the fourth column and is unaffected by the analyte on the second and seventh columns. Figure 8(c) depicts the case of the analyte adsorbed on the dielectric rods located in the fourth and seventh column of the photonic crystal. Figure 8(d) shows transmission peak shifts in the presence of all three different biomarker attachments. Different thicknesses of the analyte are represented by different colors. Clearly, our biosensor enables unmistakable and accurate detection of up to three different types of analytes, both separately and in all possible combinations.

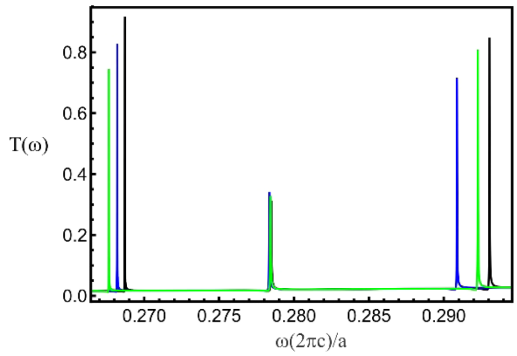

Fig. 9. Spectral fingerprints of structure presented in Figs. 1 and 2. The black line depicts transmission peaks with no biomarker adsorption. The blue line depicts transmission with 0.05a coating thickness of analyte around all rods in the second column and 0.15a thick layer thickness of analyte around all rods in the fourth column of the photonic crystal. The green line shows transmission with opposite distribution: 0.15a layer thickness of analyte around all rods in the second column and 0.05a thick layer of analyte around all dielectric rods in the fourth column.

4. BIOSENSOR PERFORMANCE WITH FURTHER PILLAR HEIGHT REDUCTION

Fabrication of a photonic crystal biosensor may be simplified if the nanopillar height can be further reduced. If the silicon rod heights are simply reduced from 2a to 1a in our design described in Sections 2 and 3, the amount of incident light guided through the photonic crystal region is insufficient to resolve transmission resonances compared to light transmitted above and below the photonic crystal. The coupling of incident light from the source into the photonic crystal can be improved by introducing a thin silicon backing layer between the silicon nanopillars and the glass substrate. In the case of a previously studied [14] biosensor design, it was shown that such a design modification enables nanopillar height reduction from 6a to 3a. In this section we explore the efficacy of introducing a thin silicon backing layer of height 0.3a to improve guiding of incident light through a photonic crystal with (reduced) nanopillar height of 1a.

Our reduced-height pillar structure backed with 0.3a silicon layer is depicted in Fig. 10. This architecture has six discernable transmission resonances at frequencies 0.293204, 0.28029, 0.27203, 0.264132, 0.254034, and 0.250172 ($2\pi c/a$). The first three resonances act similarly to those of our 2a-height structure without an extra dielectric backing layer, shown in Figs. 1 and 2. The three highest resonant frequencies, 0.293204, 0.28029, and 0.27203 ($2\pi c/a$) (see Fig. 11), act almost independently, and we chose them for biosensing. As can be seen in Fig. 11 (blue line), a large amount of nonresonant light reaches the detector at the beginning of the simulation by propagating above and below the photonic crystal region. Nevertheless, a discernable amount of resonant light reaches the detector at a later time by tunneling through the PBG created by the reduced-height photonic crystal. The total detected light (integrated overall all time) exhibits a broadband spectrum, punctuated

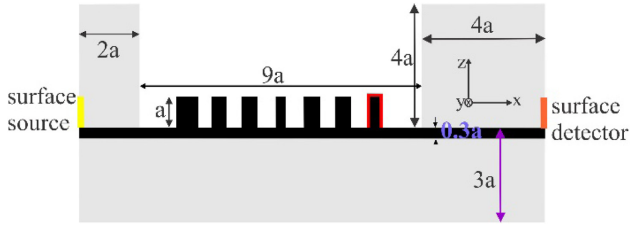

Fig. 10. The reduced-height photonic crystal is similar to that presented in Figs. 1 and 2. The difference is that the height of the silicon nanopillars is now 1a instead of 2a. However, a 0.3a layer of silicon is also embedded below the photonic crystal. This structure exhibits three optical transmission resonances as presented in Fig. 13. These resonances correspond to spatially localized optical modes within the partially formed PBG as depicted in Figs. 12(a)–12(c). Additional transmission resonances appear at lower frequencies, corresponding to more delocalized modes [see Figs. 12(d)–12(f)].

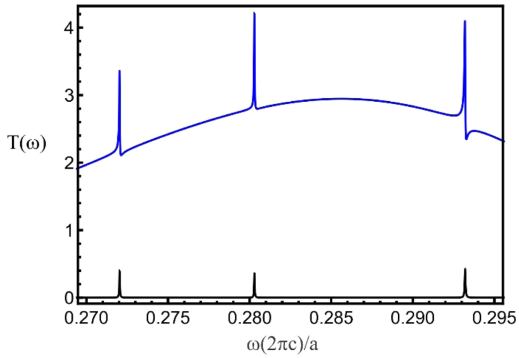

Fig. 11. Transmission spectrum of the photonic crystal biosensor presented in Fig. 12. The blue line shows the total detected light as a function of frequency (including those parts of the input pulse that bypass the photonic crystal). The black line depicts the same transmission spectrum but with the detector turned on slightly later, after the uncoupled part of the input pulse is gone. This eliminates the broadband background resulting from nonresonant light bypassing the photonic crystal. Here we present just three transmission resonances that we utilize for biosensing.

by sharp peaks at the photonic crystal resonances (Fig. 11 blue curve). Very large transmission is expected as the silicon backing layer extends from the source to the detector and represents an index guiding trajectory for the light. Overall, a larger fraction of emitted light reaches the detector than in either the case of a homogenous medium made of glass only or the case of a 2a-height photonic crystal without a silicon backing layer. By gating the detection to first allow the nonresonant light to pass and including only light that arrives at a later time, it is possible to obtain a transmission spectrum for light that interacts more fully with the photonic crystal (Fig. 11 black line).

As in Section 3, we define the limit of detection as the thickness of biomarker coating required to shift a transmission peak by one FWHM. It is apparent from the data presented in Table 2 that the device of Fig. 12 has slightly lower sensitivity than its counterpart with nanopillars of height 2a. Nevertheless, the biosensor of Fig. 12 retains a limit of detection below 0.01a analyte layer thickness.

As a consequence of the resonant illumination patterns presented in Figs. 12 and 13, the separate analyte bindings

Table 2. Frequency Shift of the Corresponding Resonances Due to 0.05a Analyte Coating Thickness, Measured in Units of FWHM, Indicated by $\Delta\omega_0$ in the Table[a]

Rods with Analyte in	Relevant ω_0	Relevant $\omega_{0.05}$	$\omega_0 - \omega_{0.05}$	$\Delta\omega_0$ at Half Max. FWHM
Second column	0.27203	0.271685	7.5 $\Delta\omega_0$ (0.0067a)	0.000046
Seventh column	0.28029	0.279929	9.025 $\Delta\omega_0$ (0.0055a)	0.00004
Fourth column	0.293204	0.292667	9.1 $\Delta\omega_0$ (0.0055a)	0.000059

[a]We include (in brackets) the thickness of the analyte layer required to shift each transmission peak by one FWHM. The original (table column 2) and shifted (table column 3) resonance frequencies are expressed in units of $(2\pi c/a)$.

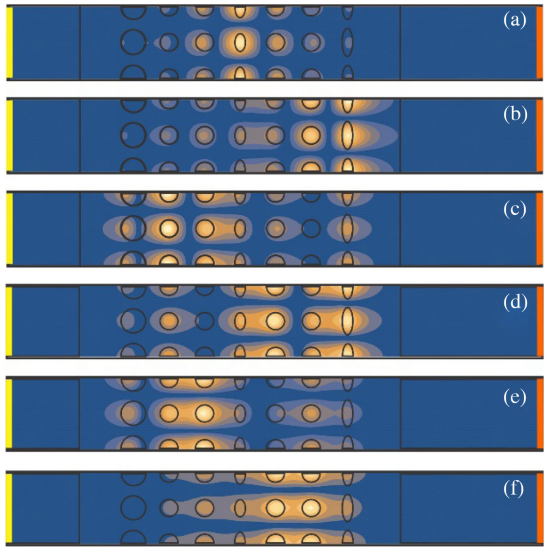

Fig. 12. Resonant illumination of the height-1a biosensor presented in Fig. 10. (a) Electric field intensity of light oscillating at frequency 0.293204 $(2\pi c/a)$ in the middle of the structure. Since the most strongly illuminated are rods in column 4, we functionalize this column to bind a layer of the first analyte around those rods. (b) Electric field intensity of light oscillating at frequency 0.28029 $(2\pi c/a)$ inside the photonic crystal. For this frequency, a second analyte should form a coating around the elliptic rods in column 7. (c) Electric field intensity of resonant light oscillating at frequency 0.27203 $(2\pi c/a)$ inside the photonic crystal. The most strongly illuminated rods are in the second column, and a third analyte layer is allowed to bind around them. In parts (d), (e), and (f) we present resonant illumination for three additional modes outside the spectral range used for biomarker detection. (d) Intensity of light oscillating at frequency 0.264132 $(2\pi c/a)$. (e) Intensity of light oscillating at frequency 0.254034 $(2\pi c/a)$. (f) Intensity of resonant light oscillating at frequency 0.250172 $(2\pi c/a)$.

are targeted for the fourth, seventh, and second columns of dielectric rods. We now consider the biosensing capability of this height-1a photonic crystal. First, the transmission peak shifts with analyte attached to dielectric rods in only one of three functionalized columns are presented in Fig. 14. Here different colors represent different analyte coating thicknesses, starting

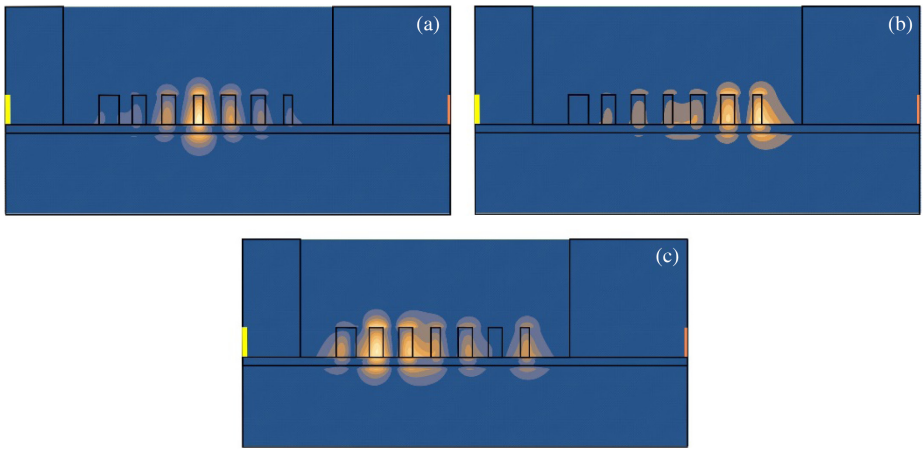

Fig. 13. Resonant illumination of the height-1a biosensor projected onto a vertical plane cutting the middle of the nanopillars presented in Fig. 10. (a) Intensity of light oscillating at frequency 0.293204 ($2\pi c/a$). (b) Intensity of light oscillating at frequency 0.28029 ($2\pi c/a$). (c) Intensity of light oscillating at frequency 0.27203 ($2\pi c/a$).

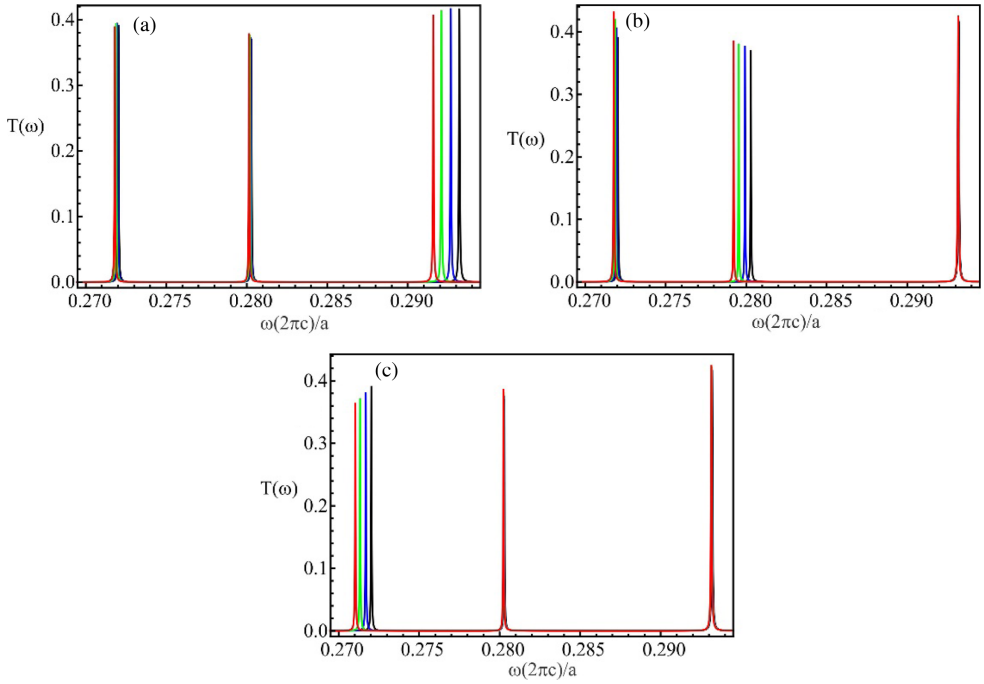

Fig. 14. Resonant transmission peaks and their shifts for light oscillating inside the structure for three coating thicknesses of analyte around dielectric rods in the (a) fourth column, (b) seventh column, and (c) second column. Black line, without analyte; blue line, rods have 0.05a layer thickness of analyte; green line, rods have 0.1a layer thickness of analyte; and red line, rods have 0.15a layer thickness of analyte.

from a 0.05a layer (blue) up to a 0.15a layer (red). Each resonant peak shift is dominantly associated with one of the functionalized dielectric columns, accurately revealing the type of analyte from its binding location. Figure 14 confirms the high sensitivity and low limit of detection of this reduced-height device. For example, the analyte adsorbed on the fourth dielectric column leads to a shift of the resonant frequency oscillating at 0.293204 ($2\pi c/a$), while the shift of other two frequencies is negligible. Clearly, the spectral fingerprints shown in Fig. 14(a) accurately identify the positions of each analyte inside the photonic crystal. The magnitude of the resonant peak shifts, compared to their FWHMs, allows detection of very small changes in the amount of attached analyte. Similarly, Fig. 14(b) shows the spectral fingerprints of analyte binding to dielectric rods in the seventh column of the photonic crystal. Figure 14(c) describes the sensitivity of our device for analyte binding to the second dielectric column.

The spectral fingerprints of the biosensor with two or three columns of dielectric rods coated with different analytes are shown in Fig. 15. Figure 15(c) reveals a weak but discernable response of resonant light oscillating at frequency 0.27203 ($2\pi c/a$) to the presence of the analyte in the fourth and seventh columns. This is a consequence of the spatially extended light distribution of the resonance mode with peak intensity on

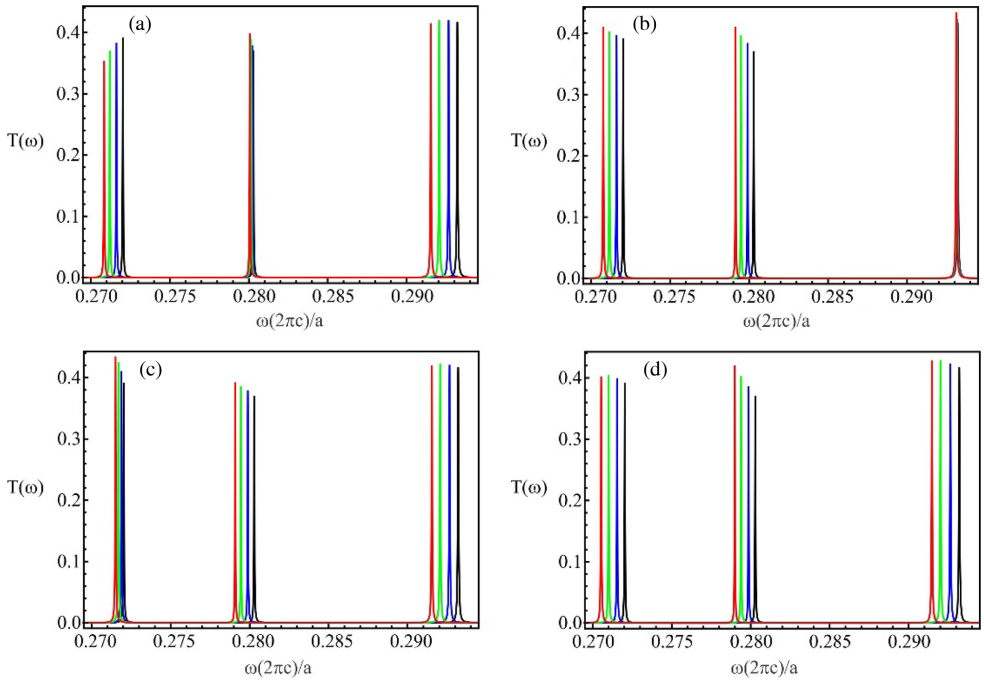

Fig. 15. Spectral fingerprints of the height-1a biosensor presented in Fig. 10 for various coating thicknesses of analyte around dielectric rods in (a) the second and fourth columns, (b) the second and seventh columns, (c) the fourth and seventh columns, and (d) the second, fourth, and seventh columns. The black line represents the transmission spectrum without analyte, the green line corresponds to 0.05a layer of analyte bound to the functionalized columns, the blue line corresponds to 0.1a layer of analyte, and the red line corresponds to 0.15a layer of analyte.

column 2 [see Fig. 12(c)]. Figures 12(c) and 13(c) show a weak overlap of this mode with the fourth and seventh columns of the dielectric rods. However, this peak shift is negligible compared to peak shifts of the other two modes. The differentiation of separate analytes is still reliable. It follows that our height-1a biosensor can still detect up to three different disease markers, not only individually but in all possible combinations.

5. CONCLUSION

We have demonstrated, by precise numerical simulations, the efficiency of an ultra-compact PBG biosensor consisting of short nanopillars. Using a square-lattice photonic crystal with the height of only one or two lattice constants, it is possible to achieve logical discrimination of three distinct disease markers, either individually or combinatorially. By expanding the spectral bandwidth for detection, relative to previous designs [12–14], it is possible to both increase the quality factor of optical resonances and reduce the required height of nanopillars constituting the photonic crystal. Remarkably, biosensor functionality is achieved with nanopillars as short as one lattice constant of the photonic crystal. This suggests that fabrication of the active region of the biosensor may be amenable to mass production methods such as nano-imprinting.

FDTD simulations of Maxwell's equations were used in our theoretical demonstration of biosensor functionality. We studied two distinct but similar devices. The first biosensor consisted of two-lattice-constant-high nanopillars, surrounded by glass below and on two sides, to form an open-top flow channel for fluid circulation. This device has three well-localized, spatially separated, optical resonance modes within the PBG, created by altering the cross sections of dielectric rods in specific columns of the photonic crystal. The second biosensor has the same design, except that the nanopillar height is reduced by a factor of two, and a thin silicon backing layer is placed between the nanopillars and the underlying glass substrate of the flow channel. This second device allows more light to propagate from the source to the detector (bypassing the photonic crystal in the vertical direction) than the first device. This leads to a significant broadband background of detected light superimposed on the transmission resonances of the photonic crystal. However, this "background noise" can be separated from the biodetection signal by temporal gating of the detected signal. The long dwell time of the light passing through the photonic crystal ensures that it reaches the detector at a later time than the broadband background light. This allows the second device to perform nearly as well as the first device for multiparametric biosensing. The device designs presented here are even more compact than previous designs [12–14] and are likely easier to fabricate for experimental testing.

Funding. Natural Sciences and Engineering Research Council of Canada (RGPIN-2019-05262); Ministarstvo Prosvete, Nauke i Tehnološkog Razvoja (171006).

Acknowledgment. Detailed numerical simulations were enabled by Compute Canada resources and the SciNet supercomputing cluster.

Disclosures. The authors declare no conflicts of interest.

REFERENCES

1. M. Liss, B. Petersen, H. Wolf, and E. Prohaska, "An aptamer-based quartz crystal protein biosensor," Anal. Chem. **74**, 4488–4495 (2002).

2. V. Pavlov, Y. Xiao, B. Shlyahovsky, and I. Willner, "Aptamer-functionalized Au nanoparticles for the amplified optical detection of thrombin," J. Am. Chem. Soc. **126**, 11768–11769 (2004).
3. E. Yablonovitch, "Inhibited spontaneous emission in solid-state physics and electronics," Phys. Rev. Lett. **58**, 2059–2062 (1987).
4. S. John, "Strong localization of photons in certain disordered dielectric superlattices," Phys. Rev. Lett. **58**, 2486–2489 (1987).
5. M. R. Lee and P. M. Fauchet, "Two-dimensional silicon photonic crystal based biosensing platform for protein detection," Opt. Express **15**, 453–4535 (2007).
6. E. Chow, A. Grot, L. W. Mirkarimi, M. Sigalas, and G. Girolami, "Ultracompact biochemical sensor built with two-dimensional photonic-crystal microcavity," Opt. Lett. **29**, 1093–1095 (2004).
7. N. Skivesen, A. Têtu, M. Kristensen, J. Kjems, L. H. Frandsen, and P. I. Borel, "Photonic-crystal waveguide biosensor," Opt. Express **15**, 3169–3176 (2007).
8. V. N. Konopsky and E. V. Alieva, "Photonic crystal surface waves for optical biosensors," Anal. Chem. **79**, 4729–4735 (2007).
9. J. Homola, S. S. Yee, and G. Gauglitz, "Surface plasmon resonance sensors: review," Sens. Actuators B Chem. **54**, 3–15 (1999).
10. B. T. Cunningham, P. Li, S. Schulz, B. Lin, C. Baird, J. Gerstenmaier, C. Genick, F. Wang, E. Fine, and L. Laing, "Label-free assays on the BIND system," J. Biomol. Screening **9**, 481–490 (2004).
11. H. Cai, M. A. Stott, D. Ozcelik, J. W. Parks, A. R. Hawkins, and H. Schmidt, "On-chip wavelength multiplexed detection of cancer DNA biomarkers in blood," Biomicrofluidics **10**, 064116 (2016).
12. A. Al Rashid and S. John, "Optical biosensing of multiple disease markers in a photonic-bandgap lab-on-a-chip: a conceptual paradigm," Phys. Rev. Appl **3**, 034001 (2015).
13. S. Feng, J. H. Jiang, A. Al Rashid, and S. John, "Biosensor architecture for enhanced disease diagnostics: lab-in-a-photonic-crystal," Opt. Express **24**, 12166–12191 (2016).
14. A. Al Rashid and S. John, "Logical discrimination of multiple disease-markers in an ultra-compact nano-pillar lab-in-a-photonic-crystal," J. Appl. Phys. **126**, 234701 (2019).
15. A. Taflove and S. C. Hagness, *Computational Electrodynamics* (Artech House, 2000).
16. K. S. Yee, "Numerical solution of initial boundary value problems involving Maxwell's equations in isotropic media," IEEE Trans. Antennas Propag. **14**, 302–307 (1966).
17. J. Vörös, "The density and refractive index of adsorbing protein layers," Biophys. J. **87**, 553–561 (2004).
18. J. A. Lewis and G. M. Gratson, "Direct writing in three dimensions," Mater. Today **7**(7-8), 32–39 (2004).
19. J. R. Raney and J. A. Lewis, "Printing mesoscale architectures," MRS Bull. **40**(11), 943–950 (2015).